Highlights

1. The RuIr@NrC is prepared by a simple and scalable one-pot pyrolysis method.
2. RuIr@NrC with RuIr alloys (~3.87 nm) on highly porous and N-rich carbon matrix.
3. RuIr@NrC showed high HER catalytic activity and stability.
4. A high mass activity is attainable, largely outperforming that of Pt/C.
5. The structural advantages and component synergy cause the high activity.

Ultrafine Ruthenium-Iridium Alloy Nanoparticles Well-Dispersed on N-rich Carbon Frameworks as Efficient Hydrogen-Generation Electrocatalysts

Jie Yu [a], Yawen Dai [a], Xinhao Wu [b], Zhenbao Zhang [a], Qijiao He [a], Chun Cheng [a], Zhen Wu [c], Zongping Shao [b, d, *], Meng Ni [a, e*]

[a] *Department of Building and Real Estate, The Hong Kong Polytechnic University, Hung Hom, Kowloon, Hong Kong 999077, China*

[b] *State Key Laboratory of Materials-Oriented Chemical Engineering, College of Chemical Engineering, Nanjing Tech University, No. 5 Xin Mofan Road, Nanjing 210009, P. R. China*

[c] *Shaanxi Key Laboratory of Energy Chemical Process Intensification, School of Chemical Engineering and Technology, Xi'an Jiaotong University, Xi'an, 710049, PR China*

[d] *Department of Chemical Engineering, Curtin University, Perth, Western Australia 6845, Australia*

[e] *Environmental Energy Research Group, Research Institute for Sustainable Urban Development (RISUD), The Hong Kong Polytechnic University, Hung Hom, Kowloon, Hong Kong 999077, China*

Corresponding author,

  (1) E-mail address: shaozp@njtech.edu.cn (Z. P. Shao)

  (2) E-mail address: meng.ni@polyu.edu.hk (M. Ni)

ABSTRACT: The production of green energy, in this case, hydrogen (H_2), from water electrolysis highly depends on the rational design of highly efficient yet cost-effective electrocatalysts for the hydrogen evolution reaction (HER). Precious-metal-based materials offer particularly prominent catalytic activities but suffer from the high cost. Thus, it is strongly desirable to develop low-metal-content composites as catalysts. In addition, fabricating an alloyed structure can greatly enhance the performance through synergy. Here, a novel nanohybrid of nanostructured RuIr alloys (~3.87 nm) with a low loading uniformly decorated on a highly porous and N-rich carbon matrix (RuIr@NrC) is constructed through a one-pot pyrolysis route. Taking advantage of the Ru/Ir single atoms, ultrafine RuIr nanostructure, high-porosity carbon substrate, and abundantly doped N, as well as their synergy, the as-formed composite demonstrates outstanding electrocatalytic performance for the HER under both basic and acidic conditions, with overpotentials of only 28 and 9 mV at 10 mA cm^{-2}, respectively. Furthermore, the as-prepared RuIr@NrC exhibits robust durability for 2000 cycles. This structure outperforms its corresponding monometallic counterparts and many typical catalytic materials and is even comparable to commercial Pt/C. Notably, a high mass activity of 6.97 A mg$_{noble\ metal}^{-1}$ is obtained, which is nearly ten times that of 20% Pt/C. This result shows the outstanding potential of RuIr@NrC for application in commercial water-splitting electrolyzers.

Keywords: ultrafine RuIr alloy; N-rich carbon matrix; a low metal loading; hydrogen evolution reaction; the component synergy

1. Introduction

Water electrolysis technology, characterized by sustainable operation and environmental benignity, is highly promising for alleviating the uneven distribution in space and time of renewable energy sources, such as wind and solar power [1-3]. Specifically, it converts the electrical power generated from sustainable energy to storable chemical energy (high-purity

2

hydrogen (H_2)). Moreover, H_2 is unanimously considered as the cleanest energy resource with the largest gravimetric energy density ($\sim$ 142 MJ kg^{-1}) in the hydrogen-economy paradigm; thus, H_2 is expected to replace fossil fuels that have negative environmental effects [4-7]. The hydrogen evolution reaction (HER) is one of the key half reactions in water electrolyzers and prevalently includes two different reaction mechanisms of the Volmer-Heyrovsky and Volmer-Tafel pathways [8, 9]. Nevertheless, this reaction suffers from a sluggish reaction rate, which results in a large applied overpotential; thus, developing efficient and low-cost electrocatalysts is of foremost significance [9-12]. To date, despite considerable advances in alternative materials, metallic platinum (Pt) still affords the best HER catalytic activity in both acidic and alkaline electrolytes [13-15]. On the basis of a HER volcano curve proposed by Trasatti et al., Pt metal is undoubtedly located at the vertex [13]. Ruthenium (Ru), with a similar M-H bond strength to Pt, also presents phenomenal Pt-like activity, as corroborated by a substantial number of studies [16-18]. However, Ir, another noble metal that also sits near the peak of the volcano plot, is relatively rarely reported as an excellent HER catalyst [19, 20]. Therefore, the use of Ir shows high promise but is a large challenge when developing ingenious designs of Ir-containing materials that provide catalytic HER activity comparable to that of Pt.

Tuning the composition by designing the alloy can efficiently modulate the electronic environment driven by the synergy of different metals, thereby diminishing the reaction energy barrier of intermediates [21-23]. As a result, a remarkably boosted electrocatalytic activity is observed. For instance, Xing's group demonstrated that alloying Pt with Ru resulted in a large decrease in the water dissociation free-energy barrier relative to Pt and subsequently optimized the hydrogen adsorption free energy compared to Ru, thus synergistically promoting HER performance [21]. Taking the fact that Ir is broadly immiscible with most metal elements in the Periodic Table, to date, only a few cases have been successfully fabricated mainly as OER and sometimes as HER catalysts, such as Ir-Rh, Ir-W, Ir-Co, Ir-Ni, and Ir-Fe alloys [24-27]. However, the synthesis recipes for some of them are relatively complicated, time/energy-

3

consuming, result in a low yield. Ru is featured with the lowest price among precious metals, being only ~ 1/12 the cost of Ir; thus, alloying Ir with Ru with broadly tunable compositions is theoretically attainable [24, 28, 29]. Accordingly, it is very appealing and highly desirable to exploit IrRu alloys with controllable compositions towards HER through a simple, flexible and high-yield preparation approach.

Downsizing the metal particle dimensions to a few nanometres together with a highly uniform distribution represents a common but useful strategy to boost the utilization of metal atoms, exposing more specific active sites and eventually leading to an obvious enhancement in electrocatalytic activity. Furthermore, a low use of the metal can maintain a balance of good cost competitiveness. To realize these goals, an excellent substrate, such as functional carbon, is commonly employed to firmly anchor metal nanoparticles, which shows plenty of structural merits for integral metal-carbon hybrids [30-33]. First, the presence of a carbon framework not only enhances the conductivity of the ensemble but also inhibits nanoparticle aggregation and improves their dispersity [34]. In addition, carbon materials always display stable anticorrosion performance, thus enhancing the stability of the total catalyst [34]. Due to the strong coupling effect, a synergy, possibly created between the metal active sites and carbon framework, induces increased catalytic activity [27]. More significantly, as demonstrated by the pioneering reports of Qiao's group or Chen's group, heteroatom (such as N) doping into carbon architectures can efficiently tune the electronic structure and create more active defects to promote H* adsorption/desorption, thus boosting hydrogen generation [27, 35, 36]. Taken together, integrating ultrasmall and highly uniform metal nanoparticles with a N-rich carbon support is reasonably expected to deliver favourable HER catalytic behaviour.

Motivated by all of the above considerations, herein, we employ a simple and scalable one-pot pyrolysis approach to rationally design an unexplored Ir-based composite material consisting of ultrafine ruthenium-iridium (RuIr) alloy nanoparticles that are well dispersed on a nitrogen (N)-rich carbon skeleton (RuIr@NrC) for efficient hydrogen production in both

4

alkaline and acidic electrolytes. Specifically, the optimized RuIr@NrC nanohybrids offer the best electrocatalytic HER activity among all the as-made electrocatalysts and robust stability, featuring low overpotentials of 28 and 9 mV at a current density of 10 mA cm^{-2} and small Tafel slopes of 35 and 51 mV dec^{-1} in 1 M KOH and 0.5 M H$_2$SO$_4$, respectively. These results are clearly superior to those of single-metal counterparts (Ir@NrC and Ru@NrC) and comparable with those of commercial Pt/C. Notably, the mass loading of the total metal in this catalyst is low, approximately only 3 wt%. Hence, a high mass activity is attainable while largely outperforming that of Pt/C. According to experimental investigations, such excellent catalytic performance might originate from structural advantages and component synergy, that is, the Ru/Ir single atoms, strong electron interaction between Ru and Ir, ultrafine RuIr nanostructures, highly porous carbon supports, and a great deal of N dopants, as well as their synergistic action.

2. Results and Discussion

The one-pot synthesis procedure of the RuIr@NrC hybrid is schematically depicted in **Scheme 1**. Briefly, a certain amount of melamine and glucose was well dispersed into a mixed aqueous solution of RuCl$_3$ and IrCl$_3$ under continuous magnetic stirring, followed by the injection of an ethylenediaminetetraacetic acid (EDTA) aqueous solution. After water removal at 60 °C for a certain time, the as-obtained solid powder was pyrolyzed in a N$_2$ flow at high temperature. Herein, glucose and EDTA acted as the carbon sources, while melamine performed both the functions of a soft template to form the abundant pores and a high surface area and N contributor to introduce abundant N species in the final product. Upon heating, melamine was first polymerized into graphitic carbon nitride layers (g-C$_3$N$_4$) at the meso-low temperature stage of less than 600 °C and then further decomposed into a N-doped carbon matrix with EDTA and glucose at elevated temperatures [37]. Concurrently, the conversion of highly charged metal ions into RuIr alloy nanoparticles (NPs) was accompanied in a carbothermal reduction environment. Due to the confined effect, the carbon skeleton could effectively prevent in situ-

5

generated metallic NPs from the undesirable agglomeration, leading to their ultrafine size and extremely high dispersity [37]. Notably, the present one-pot method, by virtue of its simple operation and scalable production capability, is highly suitable for practical industrial applications.

The particulate micromorphology of the as-obtained RuIr@NrC hybrid was first revealed through typical scanning electron microscopy (SEM) images in **Fig. 1a**. Clearly, plenty of nanoflakes were randomly stacked together to form an interconnected network, and most of them exhibited a crumpled structure. According to a previous study, such a microstructure was highly related to the use of the melamine soft template [38]. Furthermore, transmission electron microscopy (TEM) analysis displayed that many ultrasmall nanoparticles with an average size of approximately 3.87 nm were highly and uniformly anchored on the carbon architecture (**Figs. S1a** and **1b**), while the substrate featured a graphitic nature with curled layer planes, as indicated by white arrows (**Fig. 1b**). The lattice distance of these nanoparticles was measured to be about 0.207 nm, as shown in **Fig. 1c**, which was well assigned to the (101) facet of a RuIr alloy in hexagonal close packing (HCP). While, no lattice fringe space of metallic Ir was observed. To better confirm this result, we further carried out HR-TEM characterization again. The same conclusion was obtained, as shown in **Fig. S1c**. According to the typical X-ray diffraction (XRD) pattern in **Fig. S1d**, apart from two broad characteristic peaks at ~25 and 42º from the carbon support, no obvious diffraction peaks of the RuIr alloy were obtained, which disclosed the ultrasmall crystalline sizes of the RuIr alloy and their good dispersion on the substrate, corresponding to the TEM findings [30]. From the view of electrocatalysis, such ultrasmall and well-dispersed nanocrystals could offer numerous active sites and the interconnected carbon framework guaranteed efficient electron transfer, thus favouring hydrogen production [39, 40]. In addition, for sake of further and better confirming the formation of RuIr alloy NPs, a control sample, named b-RuIr@NrC (see the Experimental Section for details), was prepared. According to its corresponding XRD pattern in **Fig. S1e**, the diffraction peaks were well

6

indexed to the *hcp* RuIr alloy without any metallic Ir, which could indirectly and well imply the formation of RuIr alloy in RuIr@NrC. On the basis of energy-dispersive X-ray (EDX) spectroscopy as described in **Fig. 1d**, an Ir/Ru mass ratio of ~1.25 was observed, which was very close to the initial stoichiometric value of ~1.32. Besides, the corresponding EDX elemental maps in **Fig. 1e and f** demonstrated the homogeneous distribution of all elements (Ir, Ru, N, C) in the selected area, and the Ru and Ir atoms evenly covered the carbon substrate.

To emphasize the importance of the alloy composition on the subsequent electrocatalytic performance, hybrids of monometal Ru or Ir loaded on the carbon support with abundantly doped N (denoted as Ru@NrC or Ir@NrC) were produced as reference samples by following a similar route as that of RuIr@NrC, except that the total metal precursor was replaced with $IrCl_3$ and $RuCl_3$, respectively. At the same time, for comparison, a metal-free sample (defined as NrC) was also synthesized in the absence of metal sources during pyrolysis. Some fundamental microstructural information of these samples was obtained by the corresponding XRD patterns and SEM images in **Fig. S2**. Similar to the finding in the RuIr@NrC sample, the XRD patterns of Ru@NrC and Ir@NrC showed only two reflection peaks from carbon and suggested ultrafine particle sizes and a high dispersion degree. In addition, the broad peaks at about 25º in all samples were well attributed to graphitic carbon. All corresponding SEM images shown in **Fig. S2** revealed that these as-formed samples presented a networked architecture similar to that of the RuIr@NrC hybrid. Furthermore, Raman analysis was conducted to detect the lattice defects of the carbon support in the three as-prepared composites. As shown in **Figs. 2a and S3**, all Raman spectra featured two prominent peaks at 1336 cm^{-1} for the disordered carbon-caused D band, and 1568 cm^{-1} for the graphitic carbon-caused G band. The value of I_D/I_G (an intensity ratio between the D band and G band) could appropriately reflect the degree of defects and graphitization in the carbon architecture [41]. A similar I_D/I_G value of nearly 1.07 was found for the four as-prepared materials, indicating an analogous defect/graphitization composition with more lattice defects in these carbon frameworks. It is

7

well known that, under the circumstance of sufficient conductivity from graphitic carbon, more carbon defects are good for the HER process [42]. From the above results, it was demonstrated that the different metal compositions (Ir, RuIr, Ru, and without metal) of the four samples actually made a negligible difference in regard to the microscopic interconnected carbon networks (including the morphology and defect/graphitization formation). As determined by inductively coupled plasma atomic emission spectrometry (ICP-AES) experiments, the Ru and Ir metal contents in RuIr@NrC were 1.37 and 1.62 wt %, respectively, which agreed with the EDX spectrum results. Moreover, the amounts of Ir and Ru in Ir@NrC and Ru@NrC were estimated to be 3.44 and 2.83 wt%, respectively. Note that similar metal loadings among the three samples could guarantee the comparability of electrocatalytic behaviour. Using nitrogen adsorption-desorption experiments, the surface area (SA) and pore structure characteristics of the samples could be determined. It was apparent that the RuIr@NrC composite showed a characteristic type IV sorption isotherm with a hysteresis loop in **Fig. 2b**, thereby featuring a mesoporous nature [42, 43]. A wide pore-size distribution plot in the range of 6-20 nm was attained on the basis of the Barrett-Joyner-Halenda model (**Fig. 2c**). Accordingly, the sample displayed a large SA value of 548 m^2 g^{-1} and a high pore volume of 1.43 cm^3 g^{-1}. In view of the easier transport for reactants and availability of richer active centres, such a microstructure was of high interest for efficient HER behaviour [34, 44]. Additionally, Ir@NrC and Ru@NrC also demonstrated large surface areas and abundant mesopores (379 m^2 g^{-1} and 1.18 cm^3 g^{-1} for Ir@NrC, and 599 m^2 g^{-1} and 1.95 cm^3 g^{-1} for Ru@NrC, respectively), and these values clearly increased with the Ru/Ir weight percentages (**Fig. S4**). As for NrC, a relatively small surface area and pore volume (255 m^2 g^{-1} and 0.68 cm^3 g^{-1}, respectively) were obtained (**Fig. S4**). These findings revealed that the metal precursors of $IrCl_3$ and $RuCl_3$, especially $RuCl_3$, effectively promoted the generation of porous architectures with more mesopores. Thus, the highly mesoporous structure in RuIr@NrC may be attributed to the dual templating of melamine and metal chlorides.

8

To obtain surface chemical information, X-ray photoelectron spectroscopy (XPS) was performed on the as-formed RuIr@NrC sample, and the results were compared with those of Ru@NrC and Ir@NrC. The survey-scan spectra for all samples in **Fig. S5** clearly confirmed the co-existence of all expected elements (Ru, Ir, N, and C for RuIr@NrC; Ru, N, and C for Ru@NrC; and Ir, N, and C for Ir@NrC.). In the high-resolution Ir 4f spectrum, there were two pairs of fitted peaks, where the one at the lower energy belonged to metallic Ir (Ir^0) and the other was ascribed to oxidized Ir (Ir^{n+}) (**Fig. 2d**). Similarly, the high-resolution core spectrum of Ru 3p in **Fig. 2e** was also deconvoluted into two doublets for the metallic state of Ru (Ru^0) and oxidized Ru (Ru^{n+}). The Ir^{n+} and Ru^{n+} oxidation states were probably due to inevitable surface oxidation from the air environment [24, 30, 31]. Noticeably, relative to those in the Ir@NrC and Ru@NrC samples, the Ir 4f peaks of RuIr@NrC had a negative shift, while a meaningful positive shift was accompanied by the Ru 3p spectrum of RuIr@NrC. This result underscored the strong electron interaction between Ru and Ir. Specifically, electrons from Ru were transferred to Ir, thus resulting in higher-valence Ru and lower-valence Ir in the RuIr@NrC composite. Such an adjustment in valence state could efficiently weaken the hydrogen (H) binding strength of Ru metal sites and simultaneously enable Ir to be more prone to bind H intermediates. More significantly, previous fundamental studies demonstrated that Ru metal showed a very strong H binding ability, while Ir bound H too weakly, both of which were not favourable for the HER process [29]. Therefore, the alloying of Ru and Ir here allowed for the good optimization of hydrogen binding behaviour, and excellent HER activity was expected. **Fig. 2f** presents the N 1s spectrum of RuIr@NrC, which could be fitted to four peaks for pyridinic N (398.3 eV), pyrrolic N (399.8 eV), graphitic N (401 eV), and oxygenated N (403.3 eV), demonstrating that N atoms were successfully incorporated into the carbon framework [45, 46]. Of note, the N content in RuIr@NrC was extremely high, approximately 18.15 at%, which was much larger than that of nearly all reported N-doped carbon materials

9

[45-48]. Such N-rich doping showed great promise for the further amelioration of HER catalytic behaviour [42].

In view of the wide commercial application of alkaline water electrolyzers, we first investigated the electrocatalytic behaviour of the as-fabricated RuIr@NrC sample towards the HER in a 1 M KOH aqueous solution in a typical three-electrode cell. The catalyst loading for all tested samples remained consistent, that is, 0.464 mg cm^{-2}. First of all, to evaluate the effect of the Ru content in RuIr@NrC on the HER electrocatalytic activity, the Ru/Ir ratio was optimized in control experiments by tuning the weight ratios of ruthenium chloride and iridium chloride. Two control samples were prepared and then investigated by linear sweep voltammetry (LSV). A weight ratio of ruthenium chloride and iridium chloride of about 1 was determined to lead to optimal HER activity among all control samples (**Fig. S6**), and this ratio was then selected for the subsequent study. For comparison, some reference materials, i.e., Ir@NrC, Ru@NrC, 20 wt% Pt/C, metal-free NrC, and a bare glassy carbon (GC) electrode were also appraised in the same testing environment. **Fig. 3a** provides the LSV polarization curves of all tested samples, which were *iR-drop* corrected and relative to the reversible hydrogen electrode (RHE). As expected, no cathodic current densities were observed on the bare GC electrode, indicating its nearly-zero contribution to the HER performance. The metal-free NrC displayed an extremely poor HER activity, specifically, it required a much larger overpotential of 557 mV to drive the representative current density of 10 mA cm^{-2} (η_{10}), whereas upon integration with Ir- or Ru-based nanoparticles, the η_{10} values obtained on the formed composites (Ir@NrC and Ru@NrC) decreased dramatically to 256 and 47 mV, respectively, suggesting that metallic Ir or Ru was the dominant active site for the HER. Notably, the HER activity of Ru@NrC was much better than that of Ir@NrC, which might originate from the relatively higher intrinsic activity of Ru in a basic solution. By integrating Ru metal with Ir metal, the as-derived bimetallic RuIr@NrC hybrid presented greatly improved HER activity, and an overpotential of only 28 mV was needed to reach 10 mA cm^{-2}, which highlighted the synergistic

10

effect between Ir and Ru. As a benchmark, the Pt/C catalyst was highly active for catalyzing the HER, with an η_{10} of merely 26 mV, corresponding to that reported in the literature [49]. The similar η_{10} values between RuIr@NrC and Pt/C proved the remarkable HER activity of the RuIr@NrC sample. More importantly, it was noticeable that the current density at the large overpotential for Pt/C was clearly inferior to that of RuIr@NrC, further demonstrating the superiority of our developed catalyst. Additionally, when compared to commercialized RuO_2, the RuIr@NrC catalyst also clearly presented better HER activity (**Fig. S7**). To obtain a direct comparison, **Fig. 3c** lists the η_{10} values of the Ir@NrC, Ru@NrC, RuIr@NrC, and Pt/C samples. Tafel plots can reflect the catalytic kinetics and reaction mechanisms of electrocatalysts. As shown in **Fig. 3b**, the Tafel slope of RuIr@NrC was 35 mV dec^{-1}, which was lower than those of all control samples (Ir@NrC: 157 mV dec^{-1}, Ru@NrC: 37 mV dec^{-1}, Pt/C: 36 mV dec^{-1}, and NrC: 749 mV dec^{-1}), unveiling a faster HER process via the Volmer-Heyrovsky mechanism on the RuIr@NrC electrode [9]. Besides, the exchange current density (j_0) of a catalyst can be calculated through extrapolation of the Tafel plot. The j_0 value of RuIr@NrC was about 1.52 mA cm^{-2}, which was much higher than that of Ir@NrC and Ru@NrC (0.24 and 0.53 mA cm^{-2}, respectively) and close to the value of Pt/C (2.05 mA cm^{-2}). This result implied that the as-prepared RuIr@NrC material possessed outstanding H_2 production efficiency. Based on these typical activity-evaluation parameters, i.e., η_{10} and Tafel slope, the HER performance of the as-prepared RuIr@NrC hybrid was favourably compared to numerous previously documented representative HER electrocatalysts in alkaline electrolytes, as briefly summarized in **Table S1**. Furthermore, given that noble metals have a high cost, the mass activity (MA) in terms of the noble metal content, is of great significance for practical applications. Therefore, the MA of these studied noble metal-carbon composites was comparatively evaluated, as depicted in **Figs. S8 and 3c**. At an overpotential of 100 mV, RuIr@NrC offered a much higher MA of 6.97 A mg $_{noble\ metal}^{-1}$, nearly eighty times and two times that of the Ir@NrC and Ru@NrC catalysts

11

(0.084 and 3.91 A mg $_{\text{noble metal}}^{-1}$), respectively, as well as even approximately ten times that of the 20 % Pt benchmark (0.68 A mg $_{\text{noble metal}}^{-1}$).

As well known, the electrocatalytic activity of a catalyst is closely associated with its electrochemically active surface area (ECSA) and charge transfer resistance (R_{ct}). Here, to further illustrate the superiority of the RuIr@NrC material in the HER, the ECSA and R_{ct} values of RuIr@NrC and its monometallic counterparts (Ir@NrC and Ru@NrC) were well compared and assessed. The ECSA of the electrocatalyst was linearly proportional to its double-layer capacitance (C_{dl}), which could be obtained through cyclic voltammetry (CV) measurements at different scan rates. **Fig. S9** exhibited the CV curves of the different studied samples. From **Fig. 3d**, the as-prepared RuIr@NrC hybrid presented a C_{dl} value of 64.7 mF cm^{-2}, obviously larger than the results of Ir@NrC and Ru@NrC (33.3 and 55.1 mF cm^{-2}, respectively), revealing that the RuIr@NrC material had the most abundant catalytically active sites. When regarding 40 µF cm^{-2}, a typical reported value, as the specific capacitance [34, 47], the ECSA of RuIr@NrC, Ir@NrC and Ru@NrC were estimated to be 1602, 830, and 1355 cm^2, respectively. Whereupon, the corresponding intrinsic activities of these studied materials were also calculated by normalizing to the obtained ECSA results (**Fig. S10**). It was observed that the intrinsic activity of RuIr@NrC was still the largest among all samples. According to electrochemical impedance spectroscopy (EIS) measurements, a lower R_{ct} was also found for RuIr@NrC than for Ir@NrC and Ru@NrC (**Fig. 3e**). This result manifested that compared to the monometallic samples, the resulting RuIr@NrC sample allowed more rapid charge transfer and superior HER kinetics during the electrochemical process, which may be attributed to its porous composite architecture [40].

Apart from activity, electrochemical durability was also examined, which is indispensable for practical applications. First, continuous cyclic voltammetry (CV) was performed at a sweep rate of 100 mV s^{-1} in an alkaline electrolyte. As seen from **Fig. 3f**, the LSV curve of RuIr@NrC after 2000 cycles highly overlapped with the initial curve, demonstrating that the as-prepared

RuIr@NrC material had remarkable HER stability under alkaline conditions. The inset of **Fig. 3f** exhibits the TEM image of the cycled RuIr@NrC electrode. The well-maintained morphology after the cycling test was clearly observed, which implied the outstanding mechanical robustness of the RuIr@NrC catalyst. Additionally, a chronopotentiometric (CP) measurement also testified that the potential of the RuIr@NrC sample kept relatively stable with a decay of only approximately 40 mV after 30 h of continious operation at a fixed current density of 10 mA cm^{-2} when compared to the Pt/C benchmark (**Fig. S11**).

The HER catalytic behaviour of all given samples in acidic electrolytes was further studied. Analogous to the observation in alkaline media, the metal-free NrC was intrinsically inert towards the electrocatalytic HER in 0.5 M H_2SO_4, while the noble metal-loaded NrC samples with very little metal content (Ir@NrC, Ru@NrC, and RuIr@NrC) delivered much better catalytic properties for the acidic HER (**Fig. 3g**). Moreover, the RuIr@NrC catalyst also performed much superior catalytic activities to its monometallic counterparts, i.e., Ir@NrC and Ru@NrC, which further confirmed that the chemical combination between Ir and Ru evidently induced a catalytically synergistic effect (**Fig. 3g**). Remarkably, the η_{10} value of RuIr@NrC was just 9 mV, which was 106 and 47 mV larger than those of Ir@NrC and Ru@NrC, respectively, and was even comparable to state-of-art Pt/C (15 mV), as displayed in **Fig. 3g**. The corresponding Tafel slope values of all catalysts were determined to be 51 (RuIr@NrC), 122 (Ir@NrC), 76 (Ru@NrC), 28 (Pt/C), and 222 mV dec^{-1} (NrC) (**Fig. 3h**). Evidently, the HER process with RuIr@NrC as an electrocatalyst in acidic media was controlled by the Volmer-Heyrovsky mechanism. Shown in **Fig. 3i** compares the LSV curves of RuIr@NrC initially and after 2000 cycles. The negligible variations between the curves highlighted the excellent HER durability of RuIr@NrC under acidic conditions.

As demonstrated by previous studies, more N doping was favourable for catalyzing the HER [27, 34, 42, 50]. Ethylenediaminetetraacetic acid (EDTA) as a raw material can improve the N content of a resulting carbon-related product [37]. Thus, as expected, the as-fabricated

13

RuIr@NrC possessed a high N concentration, which could partly be responsible for the remarkable HER activity. To provide a deeper illustration of this result, a new hybrid of ultrafine RuIr alloy nanoparticles coupled with a N-doped carbon framework (named RuIr@NC) was prepared following the same route as that of RuIr@NrC, except that the EDTA precursor was replaced with glucose. XPS results showed that the total N content increased from 9.52 at% for the RuIr@NC material to 18.15 at% for the RuIr@NrC sample (**Figs. 2f and 4a**). This further supported that EDTA was beneficial to doping more N. Through deconvolution, four types of N species were clearly revealed. The relative ratios and the actual contents of the four N species are listed in **Fig. 4b**. Although the RuIr@NrC and RuIr@NC samples had nearly identical relative ratios for the four types of N species, the actual N content in RuIr@NrC were nearly twice that in RuIr@NC. Moreover, of the four types of N, the pyridinic N became the most prominent, and its content in RuIr@NrC reached 8.48 at%. It was noticeable that the N (especially pyridinic N)-enriched carbon matrix in a metal-carbon composite could offer abundant catalytically active adsorption sites for H* intermediates; more importantly, C-pyridinic N and the composited metal phase appeared to have a strong interaction, triggering the synergistic effect between the carbon structure and metal phase [27, 28, 40, 42]. The above interaction was highly likely to contribute to the activity enhancement. In addition, according to the Raman spectra (**Figs. 2a and 4c**), the I_D/I_G values for RuIr@NrC and RuIr@NC were 1.07 and 1.02, respectively, indicating more defects in RuIr@NrC, which possibly stemmed from more abundantly doped N. On this basis, as expected, the RuIr@NrC sample expressed higher catalytic activity for the HER than the RuIr@NC sample, as suggested by the lower η_{10} and Tafel slopes of 28 mV and 35 mV dec^{-1} of RuIr@NrC relative to the 74 mV and 76 mV dec^{-1} of RuIr@NC, respectively (**Figs. 4d and e**).

It should be noted that Ru and Ir single atoms are also likely produced based on the synthetic procedure, which have been known to deliver certain HER activity [51, 52]. Therefore, the aberration-corrected (AC)-HAADF-STEM measurements were also carried out on the as-

obtained RuIr@NrC hybrid to examine such a possibility. As shown in **Fig. S12a**, clearly, a large number of single atoms indeed were existed in the RuIr@NrC hybrid. To further determine the contribution from these single atoms on the HER performance, we subjected the RuIr@NrC sample to etching for removing the alloy nanoclusters; the resulting sample of which was defined as s-Ru/Ir@NrC. This is evident in the AC-HAADF-STEM image of s-Ru/Ir@NrC which presented a good deal of single atoms only (**Fig. S12b**). According to the electrochemical tests, s-Ru/Ir@NrC indeed exhibited relatively high HER activity, which but was still inferior to the original RuIr@NrC sample given its larger overpotential (**Fig. S12c**). This suggested that Ru/Ir single atoms indeed could partly be responsible for the superior HER activity while the presence of RuIr alloy nanoclusters was further effective in largely enhancing the HER activity.

In light of the above-mentioned analysis, the exceptional HER electrocatalytic property of the RuIr@NrC composite was presumably derived from the merits of its favorable chemical composition and unique nanostructure. First, Ru/Ir single atoms could make partial contribution to the as-obtained outstanding catalytic performance. Second, alloying Ru and Ir well modulated the electronic structure on the surface of the metal, thus enabling it to have an optimized H binding strength and the highest intrinsic HER activity, which in turn led to the fast kinetics of HER. Third, resulting from the confined effect of the carbon skeleton, ultrafine and highly-dispersed RuIr nanoparticles were obtained during the pyrolysis process, which promoted the effective utilization of the noble metal and provided more available catalytically active centres for the HER. More importantly, the synergistic effect created between single-atom Ru/Ir and the alloy nanoclusters also accounted for the better HER activity. Fourth, the continuous and highly porous carbon nanoarchitecture strengthened the conductivity of the catalytic material and effectively facilitated rapid charge and mass transport during the electrocatalytic process. Moreover, the above nanoarchitecture firmly immobilized an abundance of RuIr nanoparticles, thus avoiding undesired agglomeration and ensuring strong structural durability during long-term operation. Lastly, it should be pointed out that a large

number of N dopants in the carbon support highly affected the electronic environment of C and created more adsorption sites for H*, thereby further resulting in improved HER performance. In particular, pyridinic N atoms could effectively decrease the energy barrier of H* adsorption on neighbouring C atoms, which was in favor of the first-electron transfer [47].

3. Conclusion

In conclusion, here, a facile, scalable, and cost-effective one-pot pyrolysis strategy was adopted to produce a novel nanocomposite of RuIr@NrC with a very low metal concentration as a new hydrogen-generating electrocatalyst. The resultant RuIr@NrC material possessed Ru/Ir single atoms, delicately alloyed RuIr nanostructures, highly porous and conductive carbon nanoflakes, and abundant N dopants, which endowed itself with high intrinsic HER activity, more accessible active sites, boosted charge transport and mass diffusion, and favourable H adsorption/binding strength. As a result, the robust nanohybrid revealed impressive HER performance in both alkaline and acidic media, requiring small overpotentials of merely 28 and 9 mV to yield 10 mA cm^{-2}, respectively, and outstanding stability for 2000 cycles. The presented finding should arouse the great interests in the rational design of composite catalysts with ultralow amounts of precious metals while sustaining superior activity and stability; thus, these findings are highly desirable for the future growth of various energy-related fields.

Declaration of Competing Interest
The authors declare that they have no known competing financial interests or personal relationships that could have appeared to influence the work reported in this paper.

Appendix A. Supplementary data
Supplementary material related to this article can be found, in the online version, at doi:xxxxxx.

16

References

[1]   B. Rausch, M. D. Symes, G. Chisholm, L. Cronin, Decoupled catalytic hydrogen evolution from a molecular metal oxide redox mediator in water splitting, Science 345 (2014) 1326-1330.

[2]   J. Yu, Y. Zhong, X. Wu, J. Sunarso, M. Ni, W. Zhou, Z. Shao, Bifunctionality from synergy: CoP nanoparticles embedded in amorphous CoOx nanoplates with heterostructures for highly efficient water electrolysis, Adv. Sci. 5 (2018) 1800514.

[3]   Q. Gao, W. Zhang, Z. Shi, L. Yang, Y. Tang, Structural design and electronic modulation of transition-metal-carbide electrocatalysts toward efficient hydrogen evolution, Adv. Mater. 31 (2019) 1802880.

[4]   X. Zhao, H. Yang, P. Jing, W. Shi, G. Yang, P. Cheng, A metal-organic framework approach toward highly nitrogen-doped graphitic carbon as a metal-free photocatalyst for hydrogen evolution, Small 13 (2017) 1603279.

[5]   G. Zhao, K. Rui, S. X. Dou, W. Sun, Heterostructures for electrochemical hydrogen evolution reaction: a review, Adv. Funct. Mater. 28 (2018) 1803291.

[6]   J. Yu, R. Ran, Y. Zhong, W. Zhou, M. Ni, Z. Shao, Advances in porous perovskites: synthesis and electrocatalytic performance in fuel cells and metal-air batteries, Energy Environ. Mater. 3 (2020) 121-145.

[7]   J. X. Feng, J. Q. Wu, Y. X. Tong, G. R. Li, Efficient hydrogen evolution on Cu nanodots-decorated Ni_3S_2 nanotubes by optimizing atomic hydrogen adsorption and desorption, J. Am. Chem. Soc. 140 (2018) 610-617.

[8]   J. X. Feng, H. Xu, Y. T. Dong, X. F. Lu, Y. X. Tong, G. R. Li, Efficient hydrogen evolution electrocatalysis using cobalt nanotubes decorated with titanium dioxide nanodots, Angew. Chem. Int. Ed. 56 (2017) 2960-2964.

[9]   J. Zhu, L. Hu, P. Zhao, L. Y. S. Lee, K.-Y. Wong, Recent advances in electrocatalytic hydrogen evolution using nanoparticles, Chem. Rev. 120 (2019) 851-918.

[10]   L. Cao, Q. Luo, W. Liu, Y. Lin, X. Liu, Y. Cao, W. Zhang, Y. Wu, J. Yang, T. Yao, Identification of single-atom active sites in carbon-based cobalt catalysts during electrocatalytic hydrogen evolution, Nat. Catal. 2 (2019) 134-141.

[11]   L. He, W. Zhang, Q. Mo, W. Huang, L. Yang, Q. Gao, Molybdenum carbide-oxide heterostructures: in situ surface reconfiguration toward efficient electrocatalytic hydrogen evolution, Angew. Chem. Int. Ed. 59 (2020) 3544-3548.

[12]   J. X. Feng, S. Y. Tong, Y. X. Tong, G. R. Li, Pt-like hydrogen evolution electrocatalysis on PANI/CoP hybrid nanowires by weakening the shackles of hydrogen ions on the surfaces of catalysts, J. Am. Chem. Soc. 140 (2018) 5118-5126.

[13]   S. Trasatti, Work function, electronegativity, and electrochemical behaviour of metals: III. Electrolytic hydrogen evolution in acid solutions, J. Electroanal. Chem. Interfacial Electrochem. 39 (1972) 163-184.

[14]   J. Yu, Q. He, G. Yang, W. Zhou, Z. Shao, M. Ni, Recent advances and prospective in ruthenium-based materials for electrochemical water splitting, ACS Catal. 9 (2019) 9973-10011.

[15]   D. Liu, X. Li, S. Chen, H. Yan, C. Wang, C. Wu, Y. A. Haleem, S. Duan, J. Lu, B. Ge, Atomically dispersed platinum supported on curved carbon supports for efficient electrocatalytic hydrogen evolution, Nat. Energy 4 (2019) 512-518.

[16]   J. Yu, Y. Guo, S. She, S. Miao, M. Ni, W. Zhou, M. Liu, Z. Shao, Bigger is surprisingly better: agglomerates of larger RuP nanoparticles outperform benchmark Pt nanocatalysts for the hydrogen evolution reaction, Adv. Mater. 30 (2018) 1800047.

[17]   B. Lu, L. Guo, F. Wu, Y. Peng, J. E. Lu, T. J. Smart, N. Wang, Y. Z. Finfrock, D. Morris, P. Zhang, N. Li, P. Gao, Y. Ping, S. Chen, Ruthenium atomically dispersed in carbon outperforms platinum toward hydrogen evolution in alkaline media, Nat. Commun. 10 (2019) 631.

[18]   Y. Peng, B. Lu, L. Chen, N. Wang, J. E. Lu, Y. Ping, S. Chen, Hydrogen evolution reaction catalyzed by ruthenium ion-complexed graphitic-like carbon nitride nanosheets, J. Mater. Chem. A 5 (2017) 18261-18269.

[19]   T. R. Cook, D. K. Dogutan, S. Y. Reece, Y. Surendranath, T. S. Teets, D. G. Nocera, Solar energy supply and storage for the legacy and nonlegacy worlds, Chem. Rev. 110 (2010) 6474-6502.

[20]   J. Yu, X. Wu, D. Guan, Z. Hu, S.-C. Weng, H. Sun, Y. Song, R. Ran, W. Zhou, M. Ni, Monoclinic SrIrO$_3$: an easily-synthesized conductive perovskite oxide with outstanding performance for overall water splitting in alkaline solution, Chem. Mater. 32 (2020) 4509-4517.

[21]   K. Li, Y. Li, Y. Wang, J. Ge, C. Liu, W. Xing, Enhanced electrocatalytic performance for the hydrogen evolution reaction through surface enrichment of platinum nanoclusters alloying with ruthenium in situ embedded in carbon, Energy Environ. Sci. 11 (2018) 1232-1239.

[22]   G. Liu, W. Zhou, B. Chen, Q. Zhang, X. Cui, B. Li, Z. Lai, Y. Chen, Z. Zhang, L. Gu, Synthesis of RuNi alloy nanostructures composed of multilayered nanosheets for highly efficient electrocatalytic hydrogen evolution, Nano Energy 66 (2019) 104173.

[23]   M. Zhu, Q. Shao, Y. Qian, X. Huang, Superior overall water splitting electrocatalysis in acidic conditions enabled by bimetallic Ir-Ag nanotubes, Nano Energy 56 (2019) 330-337.

[24]   H. Guo, Z. Fang, H. Li, D. Fernandez, G. Henkelman, S. M. Humphrey, G. Yu, Rational design of rhodium-iridium alloy nanoparticles as highly active catalysts for acidic oxygen evolution, ACS Nano 13 (2019) 13225-13234.

[25]   H. Guo, H. Li, K. Jarvis, H. Wan, P. Kunal, S. G. Dunning, Y. Liu, G. Henkelman, S. M. Humphrey, Microwave-assisted synthesis of classically immiscible Ag–Ir alloy nanoparticle catalysts, ACS Catal. 8 (2018) 11386-11397.

[26]   F. Lv, J. Feng, K. Wang, Z. Dou, W. Zhang, J. Zhou, C. Yang, M. Luo, Y. Yang, Y. Li, Iridium-tungsten alloy nanodendrites as pH-universal water-splitting electrocatalysts, ACS Cent. Sci. 4 (2018) 1244-1252.

[27] P. Jiang, J. Chen, C. Wang, K. Yang, S. Gong, S. Liu, Z. Lin, M. Li, G. Xia, Y. Yang, Tuning the activity of carbon for electrocatalytic hydrogen evolution via an iridium-cobalt alloy core encapsulated in nitrogen-doped carbon cages, Adv. Mater. 30 (2018) 1705324.

[28] J. Su, Y. Yang, G. Xia, J. Chen, P. Jiang, Q. Chen, Ruthenium-cobalt nanoalloys encapsulated in nitrogen-doped graphene as active electrocatalysts for producing hydrogen in alkaline media, Nat. Commun. 8 (2017) 14969.

[29] J. Shan, T. Ling, K. Davey, Y. Zheng, S. Z. Qiao, Transition-metal-doped RuIr bifunctional nanocrystals for overall water splitting in acidic environments, Adv. Mater. 31 (2019) 1900510.

[30] J. Wang, Z. Wei, S. Mao, H. Li, Y. Wang, Highly uniform Ru nanoparticles over N-doped carbon: pH and temperature-universal hydrogen release from water reduction, Energy Environ. Sci. 11 (2018) 800-806.

[31] M. Ming, Y. Zhang, C. He, L. Zhao, S. Niu, G. Fan, J. S. Hu, Room-temperature sustainable synthesis of selected platinum group metal (PGM= Ir, Rh, and Ru) nanocatalysts well-dispersed on porous carbon for efficient hydrogen evolution and oxidation, Small 15 (2019) 1903057.

[32] T. He, Y. Peng, Q. Li, J. E. Lu, Q. Liu, R. Mercado, Y. Chen, F. Nichols, Y. Zhang, S. Chen, Nanocomposites based on ruthenium nanoparticles supported on cobalt and nitrogen-codoped graphene nanosheets as bifunctional catalysts for electrochemical water splitting, ACS Appl. Mater. Interfaces 11 (2019) 46912-46919.

[33] Y. Peng, W. Pan, N. Wang, J. E. Lu, S. Chen, Ruthenium ion-complexed graphitic carbon nitride nanosheets supported on reduced graphene oxide as high-performance catalysts for electrochemical hydrogen evolution, ChemSusChem 11 (2018) 130-136.

[34] T. Li, G. Luo, K. Liu, X. Li, D. Sun, L. Xu, Y. Li, Y. Tang, Encapsulation of Ni_3Fe nanoparticles in N-doped carbon nanotube-grafted carbon nanofibers as high-efficiency hydrogen evolution electrocatalysts, Adv. Funct. Mater. 28 (2018) 1805828.

20

[35]   Y. Yang, Z. Lun, G. Xia, F. Zheng, M. He, Q. Chen, Non-precious alloy encapsulated in nitrogen-doped graphene layers derived from MOFs as an active and durable hydrogen evolution reaction catalyst, Energy Environ. Sci. 8 (2015) 3563-3571.

[36]   Y. Jiao, Y. Zheng, K. Davey, S.-Z. Qiao, Activity origin and catalyst design principles for electrocatalytic hydrogen evolution on heteroatom-doped graphene, Nat. Energy 1 (2016) 1-9.

[37]   J. Yu, G. Chen, J. Sunarso, Y. Zhu, R. Ran, Z. Zhu, W. Zhou, Z. Shao, Cobalt oxide and cobalt-graphitic carbon core-shell based catalysts with remarkably high oxygen reduction reaction activity, Adv. Sci. 3 (2016) 1600060.

[38]   H. Jin, J. Wang, D. Su, Z. Wei, Z. Pang, Y. Wang, In situ cobalt-cobalt oxide/N-doped carbon hybrids as superior bifunctional electrocatalysts for hydrogen and oxygen evolution, J. Am. Chem. Soc. 137 (2015) 2688-2694.

[39]   F. Li, G. F. Han, H. J. Noh, I. Ahmad, I. Y. Jeon, J. B. Baek, Mechanochemically assisted synthesis of a Ru catalyst for hydrogen evolution with performance superior to Pt in both acidic and alkaline media, Adv. Mater. 30 (2018) 1803676.

[40]   R. Ma, Y. Zhou, Y. Chen, P. Li, Q. Liu, J. Wang, Ultrafine molybdenum carbide nanoparticles composited with carbon as a highly active hydrogen-evolution electrocatalyst, Angew. Chem. Int. Ed. 127 (2015) 14936-14940.

[41]   Q. Lu, J. Yu, X. Zou, K. Liao, P. Tan, W. Zhou, M. Ni, Z. Shao, Self-catalyzed growth of Co, N-codoped CNTs on carbon-encased CoSx surface: A noble-metal-free bifunctional oxygen electrocatalyst for flexible solid Zn-Air batteries, Adv. Funct. Mater. 29 (2019) 1904481.

[42]   Y. Zhu, G. Chen, Y. Zhong, W. Zhou, Z. Shao, Rationally designed hierarchically structured tungsten nitride and nitrogen-rich graphene-like carbon nanocomposite as efficient hydrogen evolution electrocatalyst, Adv. Sci. 5 (2018) 1700603.

21

[43]   J. Yu, Y. Zhong, W. Zhou, Z. Shao, Facile synthesis of nitrogen-doped carbon nanotubes encapsulating nickel cobalt alloys 3D networks for oxygen evolution reaction in an alkaline solution, J. Power Sources 338 (2017) 26-33.

[44]   G. Zhang, P. Wang, W.-T. Lu, C.-Y. Wang, Y.-K. Li, C. Ding, J. Gu, X.-S. Zheng, F.-F. Cao, Co nanoparticles/Co, N, S tri-doped graphene templated from in-situ-formed Co, S Co-doped g-C_3N_4 as an active bifunctional electrocatalyst for overall water splitting, ACS Appl. Mater. Interfaces 9 (2017) 28566-28576.

[45]   J. Li, Y. Song, G. Zhang, H. Liu, Y. Wang, S. Sun, X. Guo, Pyrolysis of self-assembled iron porphyrin on carbon black as core/shell structured electrocatalysts for highly efficient oxygen reduction in both alkaline and acidic medium, Adv. Funct. Mater. 27 (2017) 1604356.

[46]   J. Yu, J. Sunarso, W. Zhuang, G. Yang, Y. Zhong, W. Zhou, Z. Zhu, Z. Shao, Synthesis of highly porous metal-free oxygen reduction electrocatalysts in a self-sacrificial bacterial cellulose microreactor, Adv. Sustainable Syst. 1 (2017) 1700045.

[47]   M. Li, H. Wang, W. Zhu, W. Li, C. Wang, X. Lu, RuNi nanoparticles embedded in N-doped carbon nanofibers as a robust bifunctional catalyst for efficient overall water splitting, Adv. Sci. 7 (2020) 1901833.

[48]   J.-S. Li, Y. Wang, C.-H. Liu, S.-L. Li, Y.-G. Wang, L.-Z. Dong, Z.-H. Dai, Y.-F. Li, Y.-Q. Lan, Coupled molybdenum carbide and reduced graphene oxide electrocatalysts for efficient hydrogen evolution, Nat. Commun. 7 (2016) 11204.

[49]   Y. Liu, X. Li, Q. Zhang, W. Li, Y. Xie, H. Liu, L. Shang, Z. Liu, Z. Chen, L. Gu, A general route to fabricate low-ruthenium-based bimetals electrocatalysts for pH-universal hydrogen evolution reaction via carbon quantum dots, Angew. Chem. Int. Ed. 59 (2020) 1718.

[50]   R. Boppella, J. Tan, W. Yang, J. Moon, Homologous CoP/NiCoP heterostructure on N-doped carbon for highly efficient and pH-universal hydrogen evolution electrocatalysis, Adv. Funct. Mater. 29 (2019) 1807976.

[51]   Q. Hu, G. Li, X. Huang, Z. Wang, H. Yang, Q. Zhang, J. Liu, C. He, Electronic structure engineering of single atomic Ru by Ru nanoparticles to enable enhanced activity for alkaline water reduction, J. Mater. Chem. A 7 (2019) 19531-19538.

[52]   D. Wang, Q. Li, C. Han, Z. Xing, X. Yang, Single-atom ruthenium based catalyst for enhanced hydrogen evolution, Appl. Catal. B-Environ. 249 (2019) 91-97.
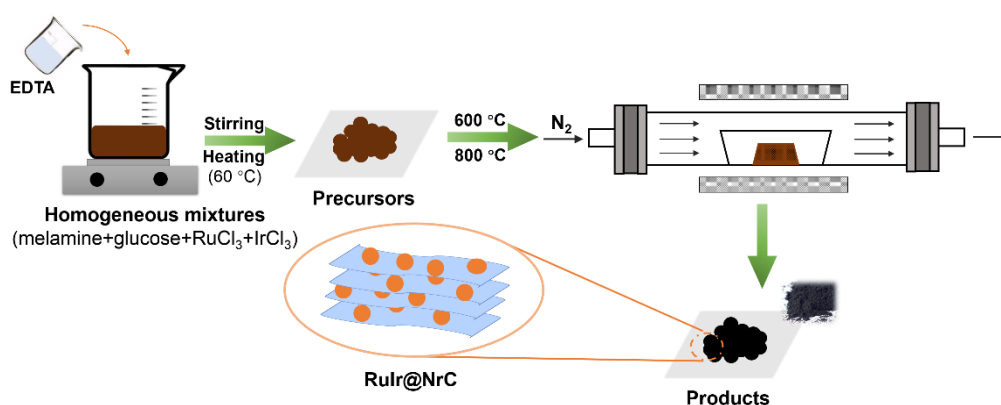
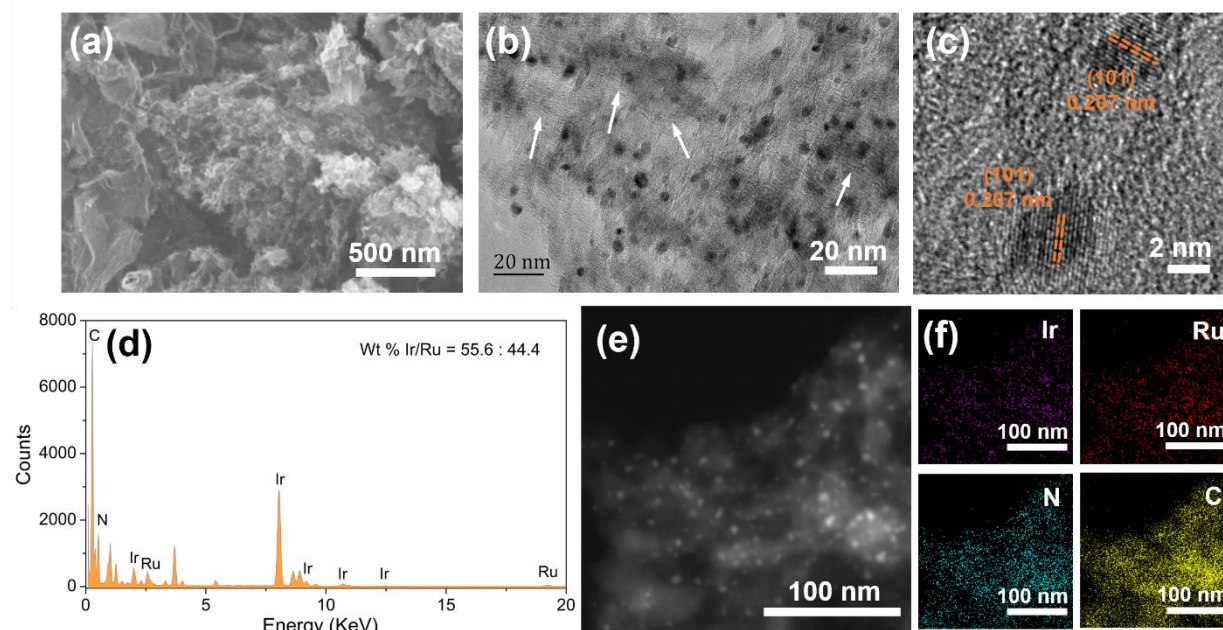**Scheme 1.** Illustration of synthesis of the RuIr@NrC hybrid.

Fig. 1. a) SEM, b) TEM, and c) HR-TEM images of RuIr@NrC. d) The EDX spectrum of RuIr@NrC. e) The high-angle annular dark-field scanning TEM (HAADF-STEM) image and f) the corresponding element mapping images (Ir, Ru, N, C) of the $Ru_{0.25}Co_{0.75}P@NPC$ sample.
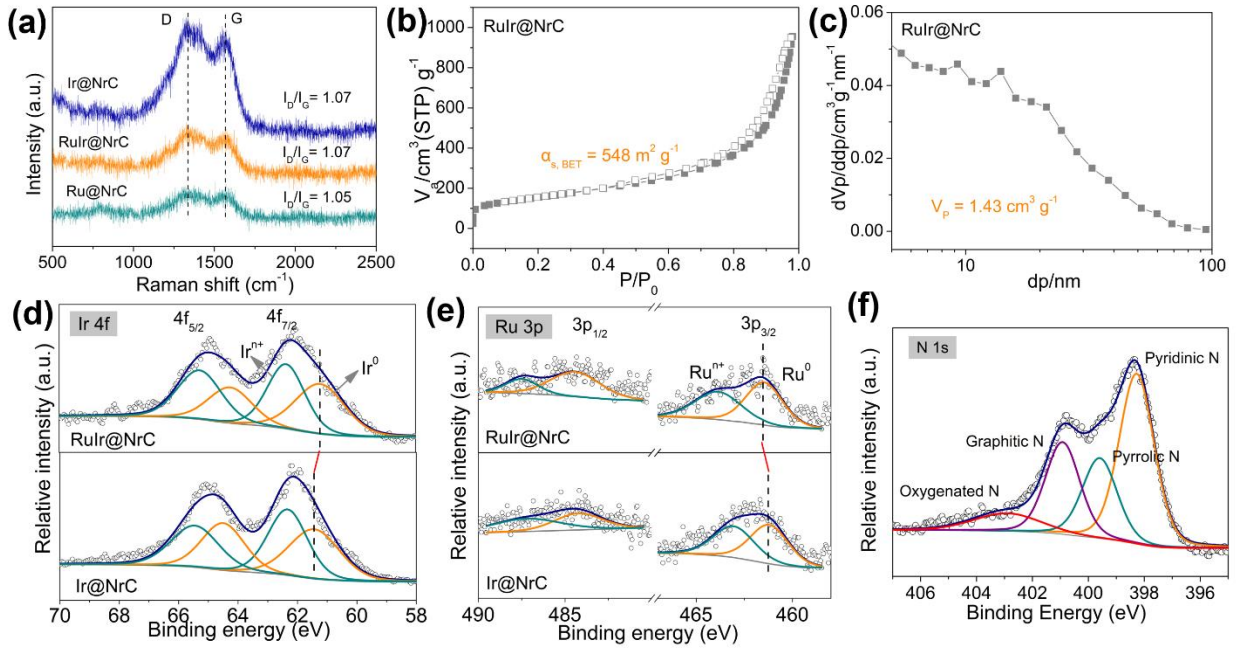
23

Fig. 2. a) Raman spectra of the RuIr@NrC, Ir@NrC and Ru@NrC catalysts. b) N_2 adsorption/desorption isotherms, and c) the corresponding pore-size distribution plot of RuIr@NrC. d) High-resolution Ir 4f XPS spectra of RuIr@NrC and Ir@NrC. e) High-resolution Ru 3p XPS spectra of RuIr@NrC and Ru@NrC. f) High-resolution N 1s XPS spectra of RuIr@NrC.
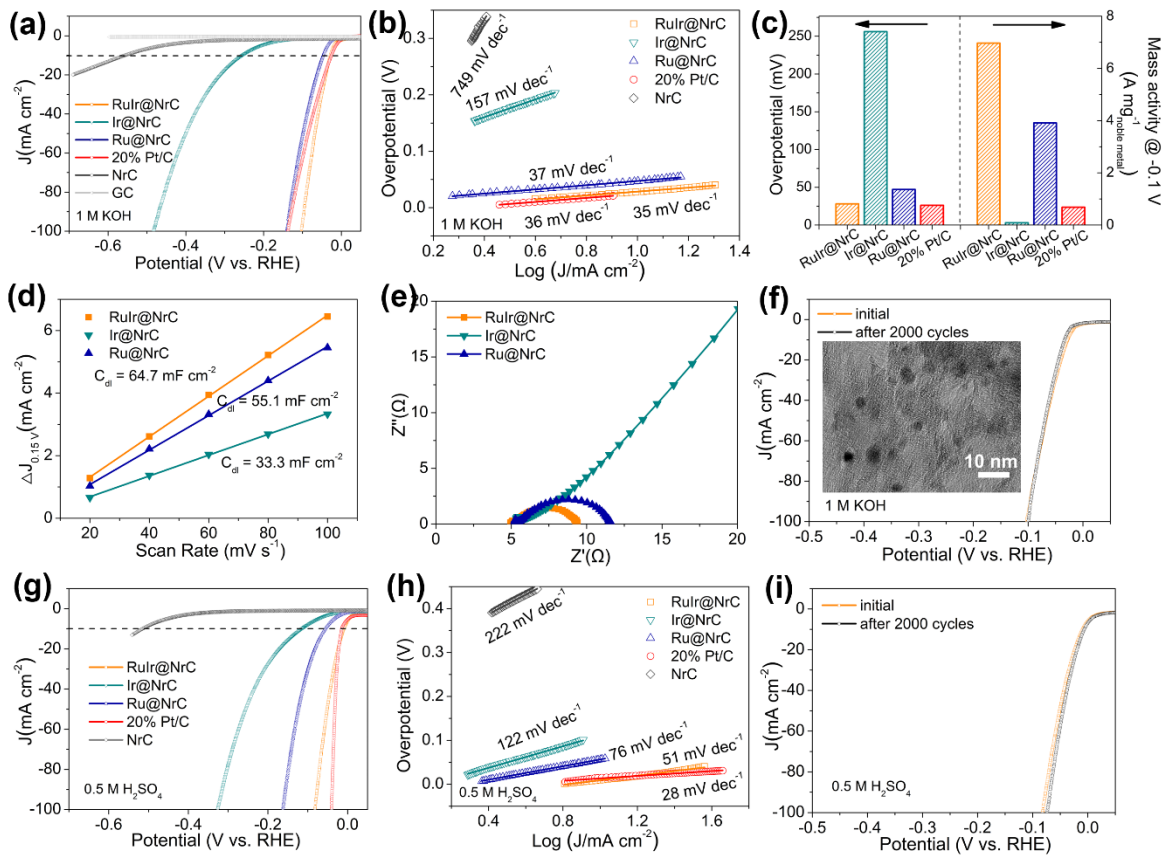

Fig. 3. a) LSV polarization curves in alkaline media (1 M KOH) and b) the corresponding Tafel plots of the RuIr@NrC, Ir@NrC, Ru@NrC, commercial 20% Pt/C, NrC, and bare GC samples.

24

c) Overpotential at the current density of 10 mA cm^{-2} (left) and the MA at the overpotential of 100 mV for these studied RuIr@NrC, Ir@NrC, Ru@NrC, and commercial 20% Pt/C catalysts. d) Capacitive current densities as a function of scan rates at 0.15 V vs. RHE, and e) Nyquist diagram at -1.1 V vs. Ag/AgCl for the three samples of RuIr@NrC, Ir@NrC and Ru@NrC. f) LSV curves initially and after 2000 cycles for this RuIr@NrC material in 1 M KOH. Inset is the TEM image of the cycled RuIr@NrC electrode. g) LSV polarization curves in acidic electrolytes (0.5 M H$_2$SO$_4$) and h) the corresponding Tafel plots of the RuIr@NrC, Ir@NrC, Ru@NrC, commercial 20% Pt/C, and NrC samples. i) LSV curves initially and after 2000 cycles for this RuIr@NrC material in 0.5 M H$_2$SO$_4$.
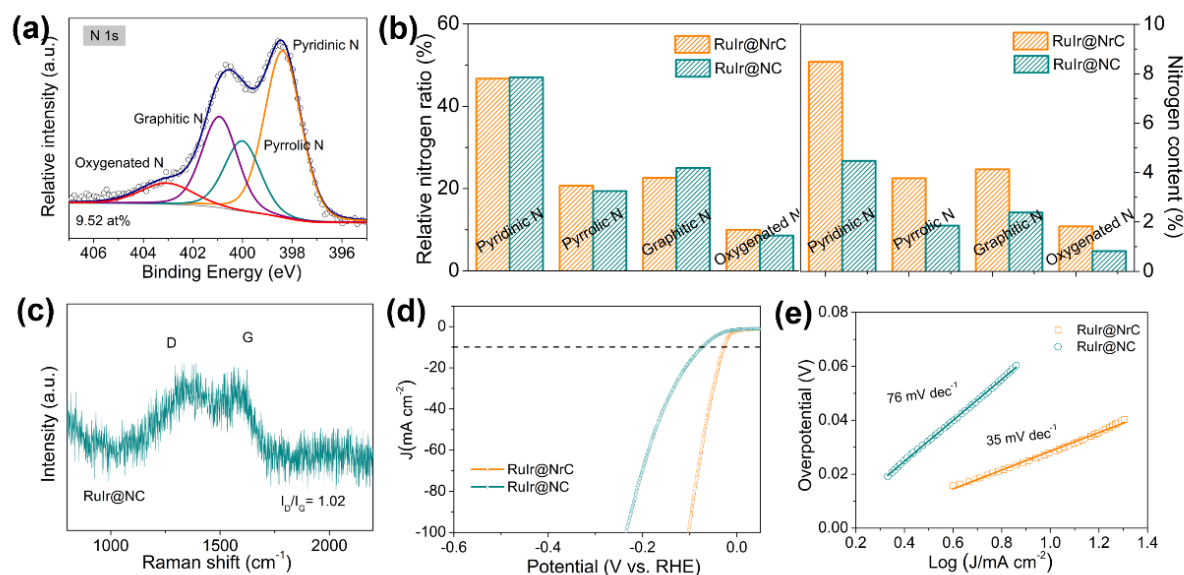

Fig. 4. a) High-resolution N 1s XPS spectra of RuIr@NC. b) The relative ratios and the actual contents for four types of N species. c) Raman spectra of the RuIr@NC catalyst. d) LSV polarization curves and e) the corresponding Tafel plots of the RuIr@NrC and RuIr@NC composites in the 1 M KOH solution.